
Proceedings of the Sixth International Conference on
Railway Technology: Research, Development and Maintenance
Edited by: J. Pombo
Civil-Comp Conferences, Volume 7, Paper 3.1
Civil-Comp Press, Edinburgh, United Kingdom, 2024
ISSN: 2753-3239, doi: 10.4203/ccc.7.3.1


# Analysis of Flow Structures in Different Loading Gaps of Freight Trains

**L. Siegel, A. Buhr, J. Bell and A. Henning**

**Institute of Aerodynamics and Flow Technology**
**German Aerospace Center**
**Göttingen, Germany**

## Abstract

In the present work, the influence of gaps in the loading scheme of a freight train on the resulting aerodynamic drag and the associated flow structures was investigated in a reduced-scale wind-tunnel experiment. The general objective of this research project is to describe the quantitative relationship between the different loading conditions and the aerodynamic drag in order to evaluate the aerodynamic optimization of the loading scheme in rail freight transport in the energy consumption balance and to enable a cost-benefit analysis for train operators with regard to factors such as logistics and others. In the present study, particle image velocimetry was used to investigate the flow structures occurring on a test container which was attached to a generic freight train model. By varying the loading scheme, different flow situations could be observed that are characteristic of selected loading configurations. Surface-pressure measurements were also carried out in order to be able to investigate the relationship between the forces occurring on the test container and the simultaneously prevailing flow structures.

**Keywords:** freight train, flow structures, bluff bodies, surface pressure distribution, aerodynamic drag, particle image velocimetry, PIV

## 1 Introduction

With the ever-increasing demand for energy efficient, low emission freight transport, the expansion and development of rail freight transport becomes a more and more relevant topic. The average $CO_2$ emissions of freight trains with 16 g/(t·km) is

multiple times lower compared to the emission of freight transport on trucks with 118 g/(t·km) [1]. With the need for a climate-friendly means of transport for an increasing amount of goods over land, the demand of higher freight train's capacity, speed and time-optimised logistical processes increases as well. Other than in the high-speed passenger train sector, the design developments of freight trains were mostly limited to structural or logistical aspects in the past. Especially the optimization of logistical processes like commissioning for different destinations can lead to significant gaps of one or multiple missing containers in the overall loading scheme. The crucial information for train operators at this point is if there are certain limits to critical gap sizes and what is the estimated, quantitative effect of these loading gaps on the total energy consumption.

In a preliminary study, a detailed, incremental investigation of the influence of different loading configurations on the aerodynamic drag has already been carried out (see Figure 1) [2]. Comparable investigations of the flow causing drag from container gaps have been performed by [3,4]. Here, the loading gaps upstream and downstream of a test container, which was mounted on a 6-component strain gauge force measuring balance, were varied step by step at 0° cross-wind condition. The course of the graphs indicates different flow conditions which, depending on the loading configuration, have a stronger or weaker influence on the aerodynamic drag and lead to sometimes abrupt increases and sometimes linear changes in drag. In order to identify and evaluate the underlying flow structures, particle image velocimetry (PIV) and surface pressure measurements were carried out for selected loading gaps in the present study. Through the combined evaluation of the respective prevailing flow situation, the previously measured drag coefficients can be understood and potential for aerodynamic optimisation can be identified.

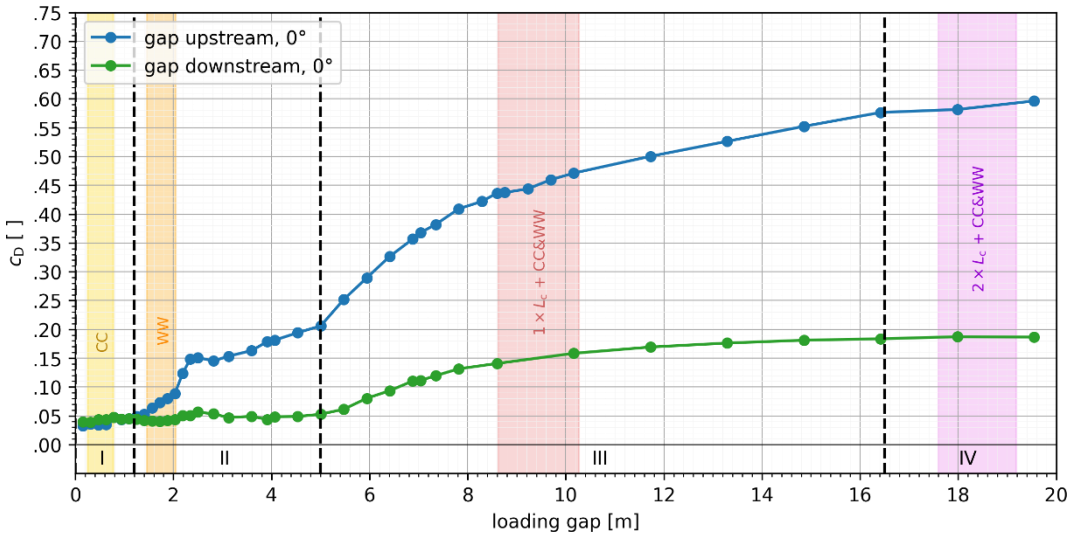


Figure 1: Aerodynamic drag coefficient of test container for gap upstream and gap downstream at 0° cross-wind condition.

# 2 Experimental Setup and Methods

## 2.1. Flow Configuration

The experimental investigations were carried out in the crosswind test facility in Göttingen (SWG), a closed-circuit, Göttingen-type wind tunnel. The test section of the SWG is 2.4 m wide, 1.6 m high and 9 m long. The design of the SWG provides wind flow speeds up to 60 m/s generated by a 500 kW fan with a low-turbulence intensity in mean flow direction of 0.25% in the core region of the test-section.
Figure 2 shows the generic freight train model on a scale of 1:15 with a length of 6.24 m in the SWG test section. For the investigation of a freight train model of this length, the model structure was positioned on a special 8.4 m long splitter plate at a height of 0.45 m to ensure a free flow outside the boundary layer that forms near the wind tunnel floor.
The model was installed on a single-track ballast and rail (STBR) to simulate realistic flow development close to the ground. Generic upstream and downstream flow bodies (black) with wheelsets (orange) were positioned in front of and behind the test area (blue) to represent flow conditions at any central position in the loading scheme. The test area consisted of a generic freight wagon base with bogies (grey), in the centre of which a test container (dark blue) with a length $L_c$ of 521 mm and a cross-sectional area of 170 mm ($B_c$) x 195 mm ($H_c$) was mounted on a 6-component strain gauge force measuring balance.
The filler parts (light blue) could be filled incrementally with block elements in order to vary the loading gaps upstream and downstream of the test container between 10.4 mm and 1303.3 mm (corresponding to 1/50 $L_c$ and 2.5 $L_c$ respectively). The Reynolds number used for the measurements was 5.5 x $10^5$ in relation to the test container width $B_c$ and the inflow velocity $U_\infty$ of approx. 50 m/s.

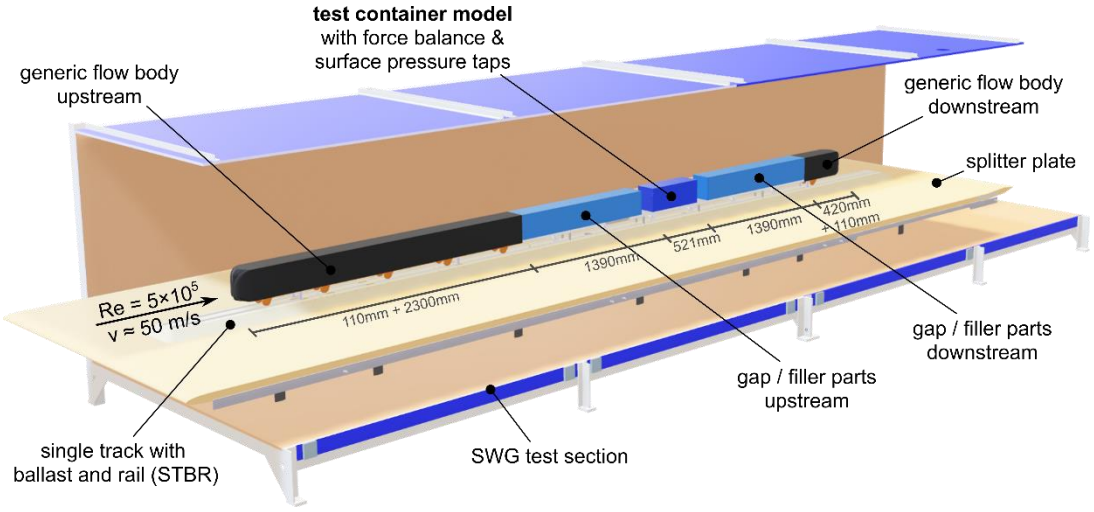


Figure 2: Measurement setup of the freight train model in the crosswind test facility in Göttingen (SWG).

The range of possible loading gaps with the combination of different wagon and swap body types is illustrated in Figure 3. The different gaps are categorized by their occurrence in the loading scheme: 'CC' for gaps between containers on the same wagon, 'WW' for gaps between containers with an inter-car gap and 1ES/2ES for gaps including one or two empty slots. The resulting gap sizes depend on the specifications of the wagon and swap bodies like wagon length, container slots, spigot positions, wagon buffer size, minimum distance to the load and the swap body length.

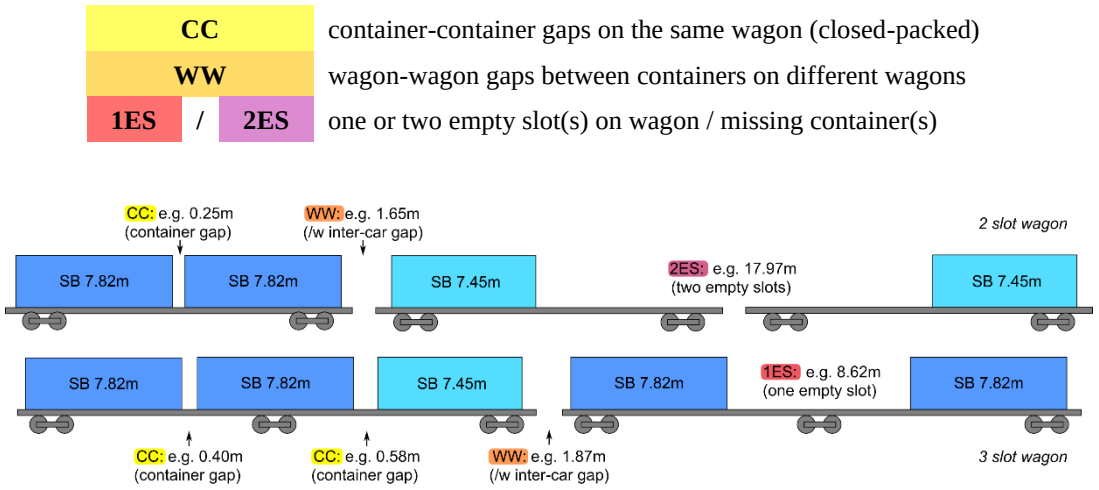


Figure 3: Characterization of gap types in a loading scheme of a freight train.

## 2.2. PIV and Surface Pressure Measurements

The velocity data were acquired using a two-dimensional, two-component PIV system (2D-2C PIV) which measured two velocity components in horizontal plane. A double-pulse laser (Q-switched Nd:YAG; Type: Innolas Spitlight 600) with a maximum energy of 350 mJ per pulse and a repetition rate of 10 Hz was used for the PIV measurements. The laser light sheet generated was coupled into the measurement area at the side of the wind tunnel wall through a glass pane. The light sheet was parallel to the floor at a height of 93.3 mm above the top edge of the rail (see Figure 4), which corresponds to a height of 1.4 m above the top edge of the rail for a test-relevant measurement height in accordance with the technical specifications for interoperability [5].

The flow was seeded with DEHS particles, the scattered light of which was recorded within the light sheet plane using two CMOS cameras (type: PCO edge 5.5). The cameras were located vertically above the light sheet behind a glass pane embedded in the wind tunnel ceiling. The cameras were arranged one behind the other in the direction of flow so that, in combination with the lenses used, a composite field of view of approximately 750 mm x 320 mm was obtained. The position of the observation windows was chosen in such a way that the flow structures could be measured from the front third of the test container upstream, which resulted from variations in the loading scheme (see Figure 5). In order to obtain meaningful statistics, 5000 double images were recorded for each configuration. The

configurations were selected on the basis of the aerodynamic drag coefficients, which were determined as part of a previous parameter study (see Figure 1).

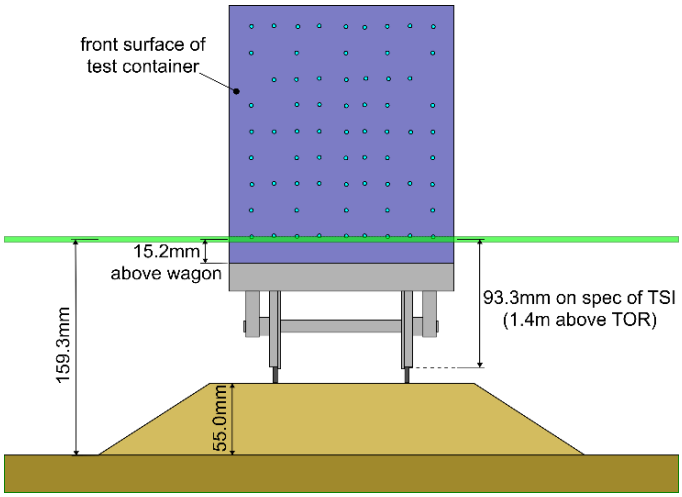


Figure 4: Sketch of the position of the laser light sheet at vertical height in the front view of the test container (green dots mark the position of the surface pressure taps).

The evaluation of the PIV data was performed using a multi-pass procedure with decreasing window size (initial window size: 96 px x 96 px; final window size: 32 px x 32 px) and a window overlap of 50%. This results in a total amount of 21,600 grid points and a grid spacing of 2.4 mm ≙ 0.014 $B_c$.
The test container was equipped with 254 pressure taps (67 taps each on front and rear, 41 taps on each side and 38 taps on the top) around the exposed surface sides to investigate the change in the flow around the test container depending on the up- and downstream gap. The pressure signals were recorded using 4 PSI modules with a sampling rate of 300 Hz and 6000 samples per configuration. The surface pressure measurements were carried out independently of the PIV measurements, as the test container was covered with a low-reflection foil during the PIV measurements to prevent unwanted reflections of the laser light sheet.

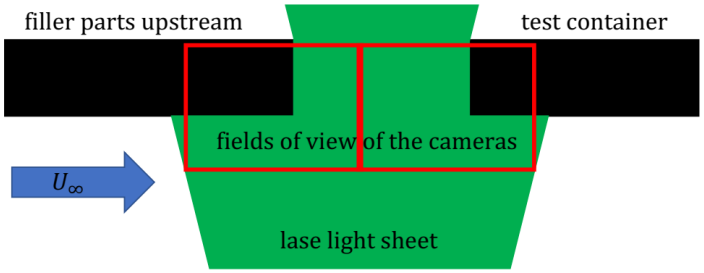


Figure 5: Schematic of the position of the laser light sheet in relation to the test container in the horizontal plane and the camera fields of view in the plan view.

# 3 Results

The measured flow fields are analyzed with regard to their characteristic topologies for selected loading configurations and compared with the corresponding surface pressure measurements. The time-averaged values are mainly considered here in order to obtain a general overview of the flow situations and because the underlying drag values are also time-averaged. In the case of the flow fields, the averaged vector fields and the color-coded vorticity $\omega_z$ are shown for each configuration (cf. Figure 6-11 a), which is calculated as follows:

$$\omega_z = \frac{\partial v}{\partial x} - \frac{\partial u}{\partial y} \tag{1}$$

Here, $u$ and $v$ are the velocity components in the plane and $x$ and $y$ are the corresponding spatial directions. Furthermore, the distributions of the respective standard deviations of the absolute velocities (cf. Figure 6-11 b) and the streamlines of the averaged velocity fields (cf. Figure 6-11 c) are shown. The contours of the test container and the various filler parts are marked in black in the figures. The axes are scaled with the test container width $B_c$, which is decisive for the occurring flow structures.
In this study, only the data of the front surface of the test container (second or downstream container in Figure 5) is used to represent the surface pressures. The averaged distributions of the surface pressures (cf. Figure 6-11 d) and the corresponding standard deviations (cf. Figure 6-11 e) are shown in each case. The vertical position of the laser light sheet is marked with a green line in these figures.

**Gap configuration 0.8 m (model dimension 52 mm ≙ 0.3 $B_c$; Figure 6):**
This gap configuration lies within the range of CC gap sizes (cf. Figure 3). Low flow velocities in the gap and a clear demarcation between the flow within the gap and the inflow can be observed in Figure 6a and 6c. The color-coded vorticity indicates a strong shear in the transition area from the gap flow to the free inflow (cf. Figure 6a). In addition, a slight asymmetry of the flow field within the gap can be observed, which is characterized by vortex formation only in the upper area of the gap (cf. Figure 6a and 6c). The standard deviation of the absolute velocities only shows a significant fluctuation at the upstream edge of the test container, while the rest of the flow field outside the boundary layer remains largely unaffected (cf. Figure 6b).
Overall, a low pressure distribution can be observed at the test container (cf. Figure 6d), which is accompanied by a relatively low drag coefficient (cf. Figure 1). Only at the upstream edges of the test container slight pressure fluctuations can be observed (cf. Figure 6e).

**Gap configuration 2.0 m (model dimension 136 mm ≙ 0.8 $B_c$; Figure 7):**
This gap configuration lies within the range of WW gap sizes (cf. Figure 3) and it is characterized by a significant increase in the drag coefficient (cf. Figure 1). The flow field shows an increased backflow area within the gap (cf. Figure 7a and c). Here, the

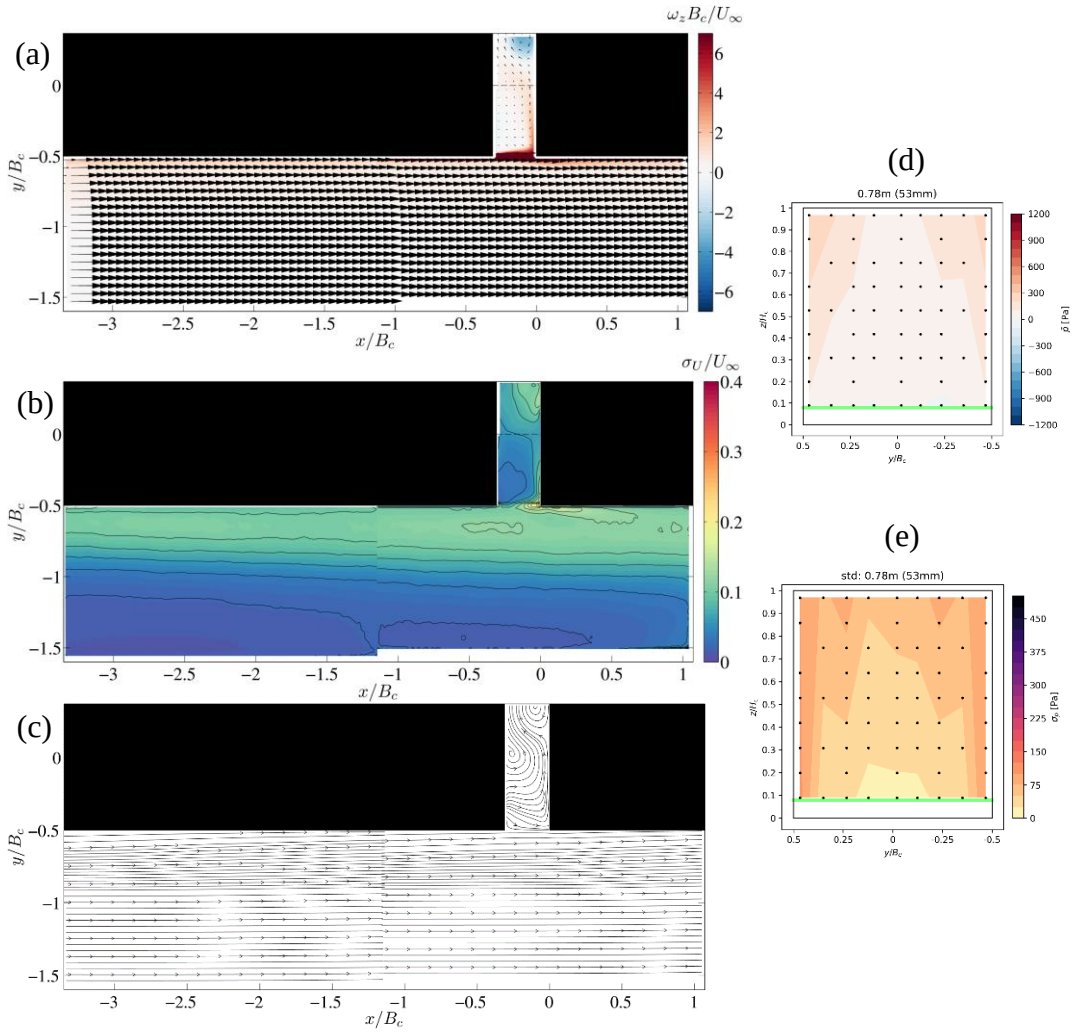


Figure 6: (a) Averaged vector field with colour-coded vorticity $\omega_z$, (b) standard deviation of the absolute velocity, (c) streamlines of the averaged velocity field, (d) averaged surface pressure distribution and (e) standard deviation of the surface pressure distribution for the gap size 0.8 m (model dimension: 52 mm).

flow impinges on the upper upstream edge of the test container, flows down the front surface and upstream in the lower area (cf. Figure 7d). Based on the averaged vector distribution and the streamlines within the gap, a clear reverse flow can thus be observed for the selected observation plane.

As the gap size increases, there is also an interaction between the incident flow and the flow within the gap, as the incident flow can now effectively enter the gap region and be deflected out of it again (cf. Figure 7a and c). This observation is also reflected in the standard deviation of the absolute velocity, for which a clearly pronounced area with increased fluctuations can be registered within the boundary layer at the level of the gap and downstream of the leading edge of the test container (cf. Figure 7b). The vorticity also indicates increased shear at the trailing edge of the filler parts and the leading edge of the test container (cf. Figure 7a). Based on the increased standard deviation of the surface pressure (cf. Figure 7e), especially at the edges of the test

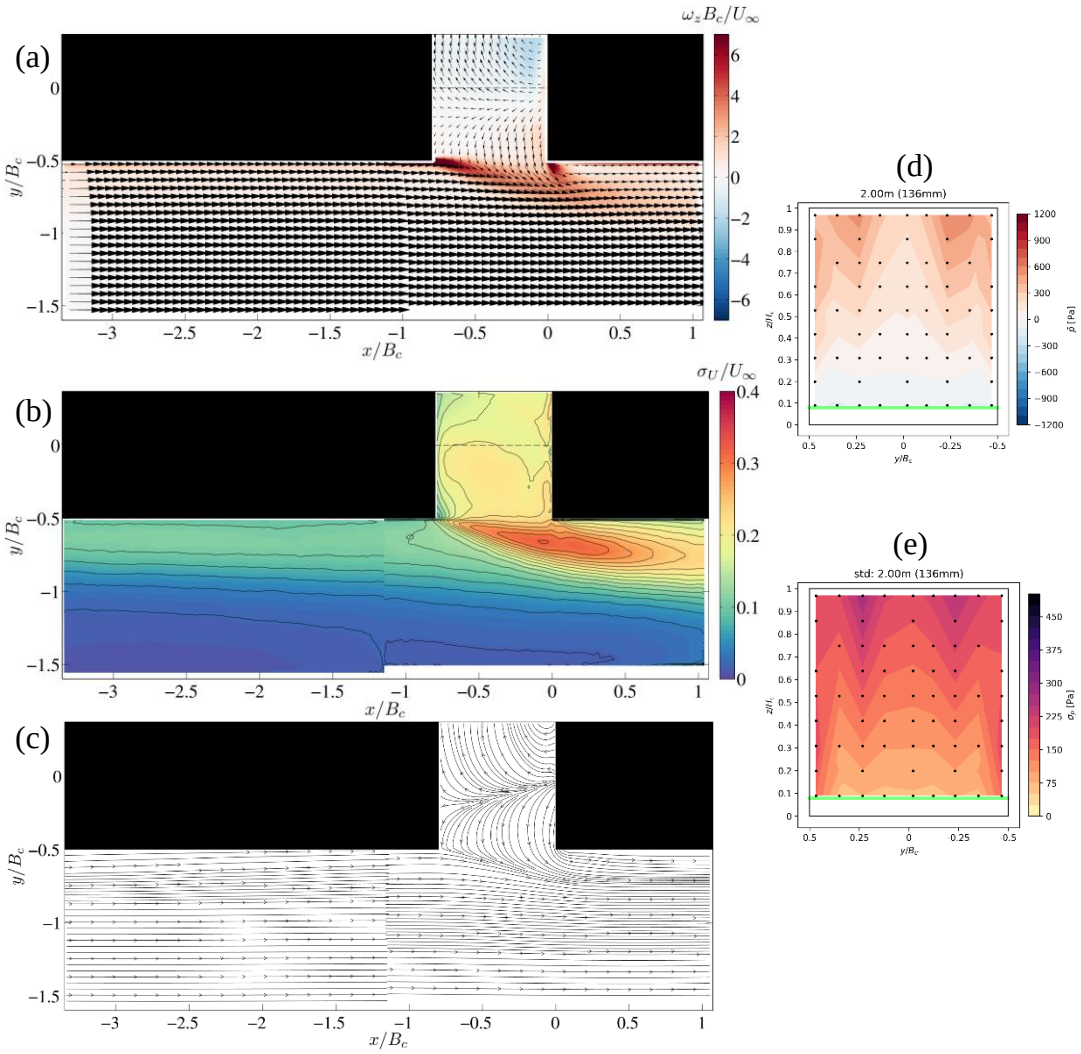


Figure 7: (a) Averaged vector field with colour-coded vorticity $\omega_z$, (b) standard deviation of the absolute velocity, (c) streamlines of the averaged velocity field, (d) averaged surface pressure distribution and (e) standard deviation of the surface pressure distribution for the gap size 2.0 m (model dimension: 136 mm).

container, the increased drag coefficient can be explained in conjunction with the observations made of the flow field as a whole.

**Gap configuration 3.9 m (model dimension 261 mm ≙ 1.5 $B_c$; Figure 8):**
This gap configuration lies within the range of a WW and 1ES gap size (cf. Figure 3) which is characterized by an almost linear profile with a comparable low gradient of the aerodynamic drag coefficient (cf. Figure 1). The flow field within the gap also has a coherent structure, which is characterized by a relatively strong reverse flow (cf. Figure 8a and c). However, individual, symmetrical vortex structures can be detected directly upstream of the test container, which are sucked around the front side edges of the test container. The mean surface pressure distribution is slightly increased over

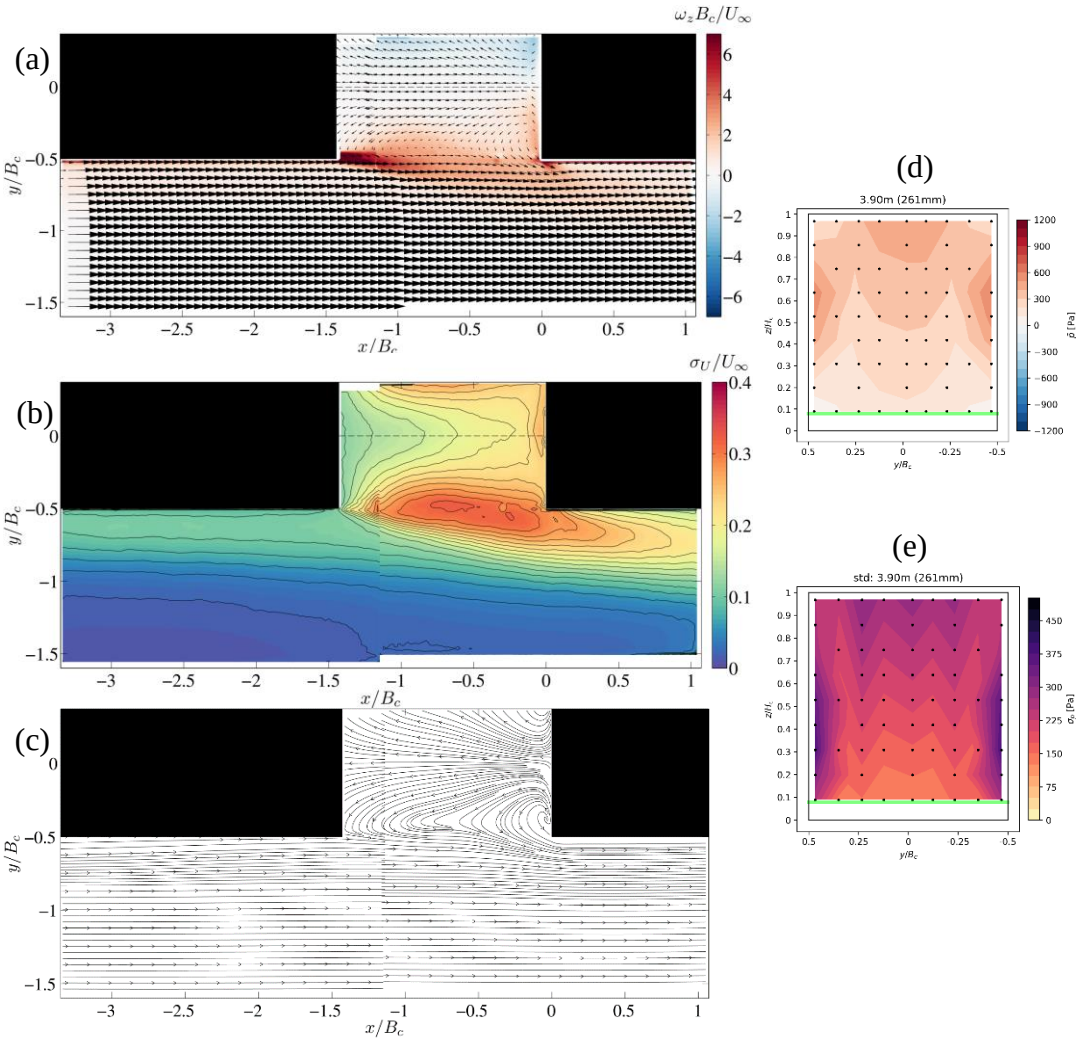


Figure 8: (a) Averaged vector field with colour-coded vorticity $\omega_z$, (b) standard deviation of the absolute velocity, (c) streamlines of the averaged velocity field, (d) averaged surface pressure distribution and (e) standard deviation of the surface pressure distribution for the gap size 3.9 m (model dimension: 261 mm).

the entire front surface compared to the previously observed gap, whereby a significant increase in pressure can be observed especially at the side edges (cf. Figure 8d).

The vorticity indicates an increased, symmetrical detachment at the trailing edge of the filler part (cf. Figure 8a), which is accompanied by increased velocity fluctuations in the detachment area downstream (cf. Figure 8b). The standard deviation of the surface pressure distribution clearly shows that the flow no longer mainly hits the test container from above and enters the gap, but also increasingly affects the test container from the side and causes an overall increase in pressure fluctuations (cf. Figure 8e). In general, however, it is on average a large continuous flow structure within the gap that mainly influences the aerodynamic drag.

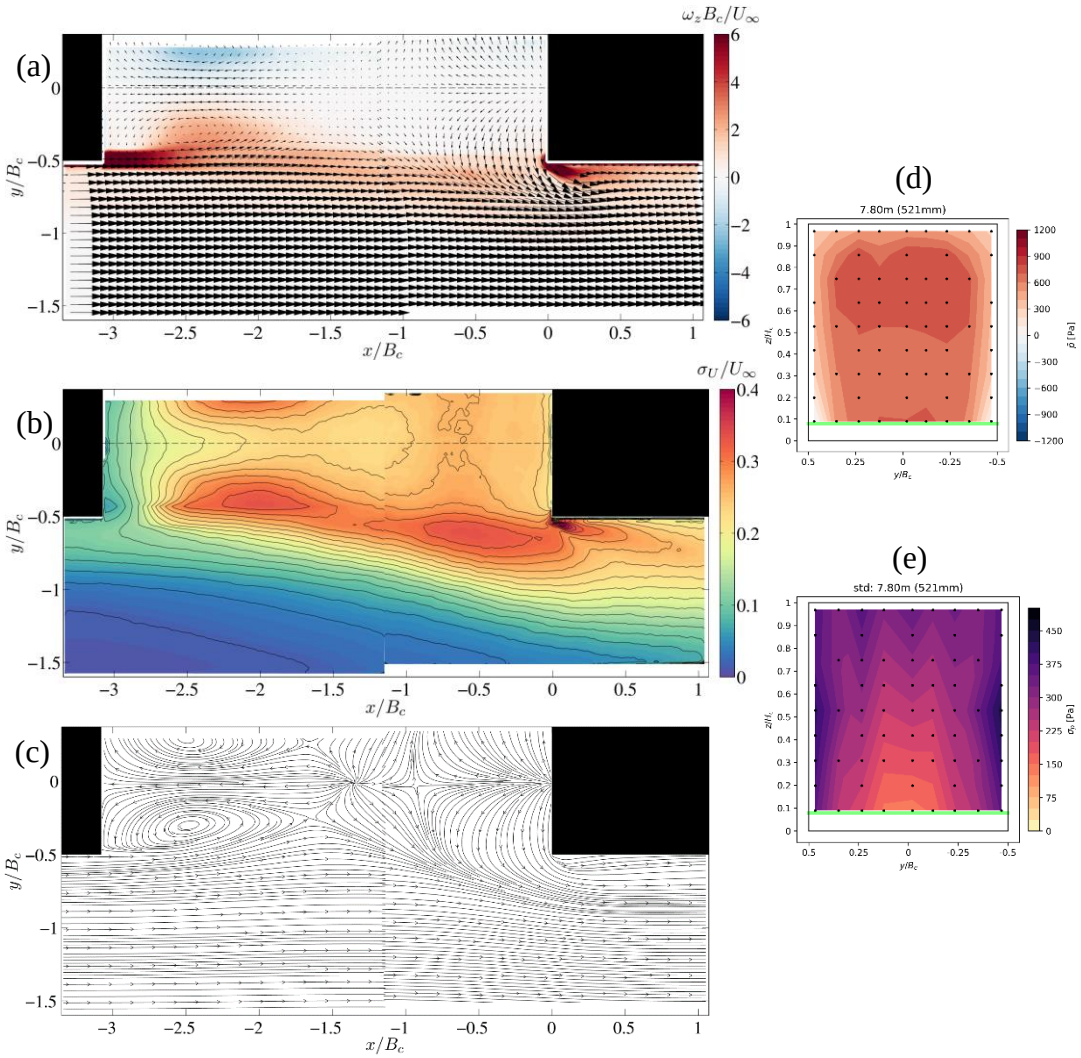


Figure 9: (a) Averaged vector field with colour-coded vorticity $\omega_z$, (b) standard deviation of the absolute velocity, (c) streamlines of the averaged velocity field, (d) averaged surface pressure distribution and (e) standard deviation of the surface pressure distribution for the gap size 7.8 m (model dimension: 521 mm).

**Gap configuration 7.8 m (model dimension 521 mm ≙ 3.1 $B_c$; Figure 9):**
This gap configuration corresponds to a gap size of 1ES (cf. Figure 3) and it is characterized by a significant change in the flow field topology within the gap. The flow structure of a continuous backflow area observed in the previous configurations is now split on average into a stagnation point flow upstream of the test container, a transition area and a symmetrical recirculation area downstream of the upstream container part (cf. Figure 9a and c). The inflow now enters the gap completely, so that it can now impinge centrally on the front surface of the test container. This is accompanied by a significant increase in the drag coefficient on the test container (cf.

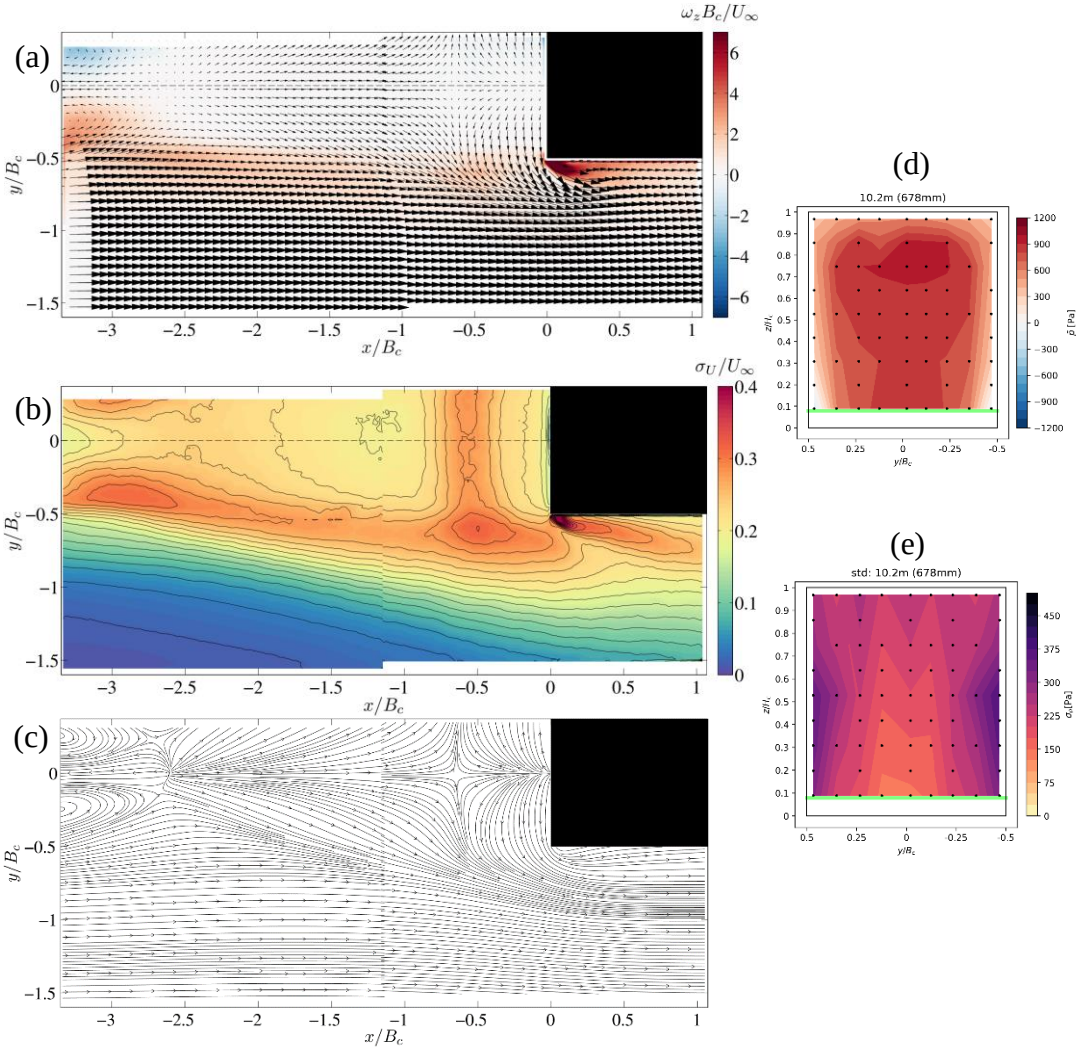


Figure 10: (a) Averaged vector field with colour-coded vorticity $\omega_z$, (b) standard deviation of the absolute velocity, (c) streamlines of the averaged velocity field, (d) averaged surface pressure distribution and (e) standard deviation of the surface pressure distribution for the gap size 10.2 m (model dimension: 678 mm).

Figure 1) as well as a significantly higher surface pressure distribution in the center of the front surface of the test container (cf. Figure 9d). At the same time, flow separation accompanied by an acceleration of the flow can be observed at the leading edge of the test container, as is typically found in the free flow around a bluff body (cf. Figure 9a and c). The observed recirculation area downstream of the upstream container also explains the increase in the drag coefficient when a gap of at least one container is left behind the test container (cf. Figure 1 green curve), as the periodic vortex shedding creates additional aerodynamic drag.

The standard deviation of the absolute velocities shows a clearly widened detachment area within and downstream of the gap as well as high velocity fluctuations at the leading edge of the test container due to the accelerated flow (cf. Figure 9b). The latter can also be observed in the distribution of the standard deviation of the surface

pressures, for which the highest pressure fluctuations of all considered configurations occur at the side edges of the test container (cf. Figure 9e).

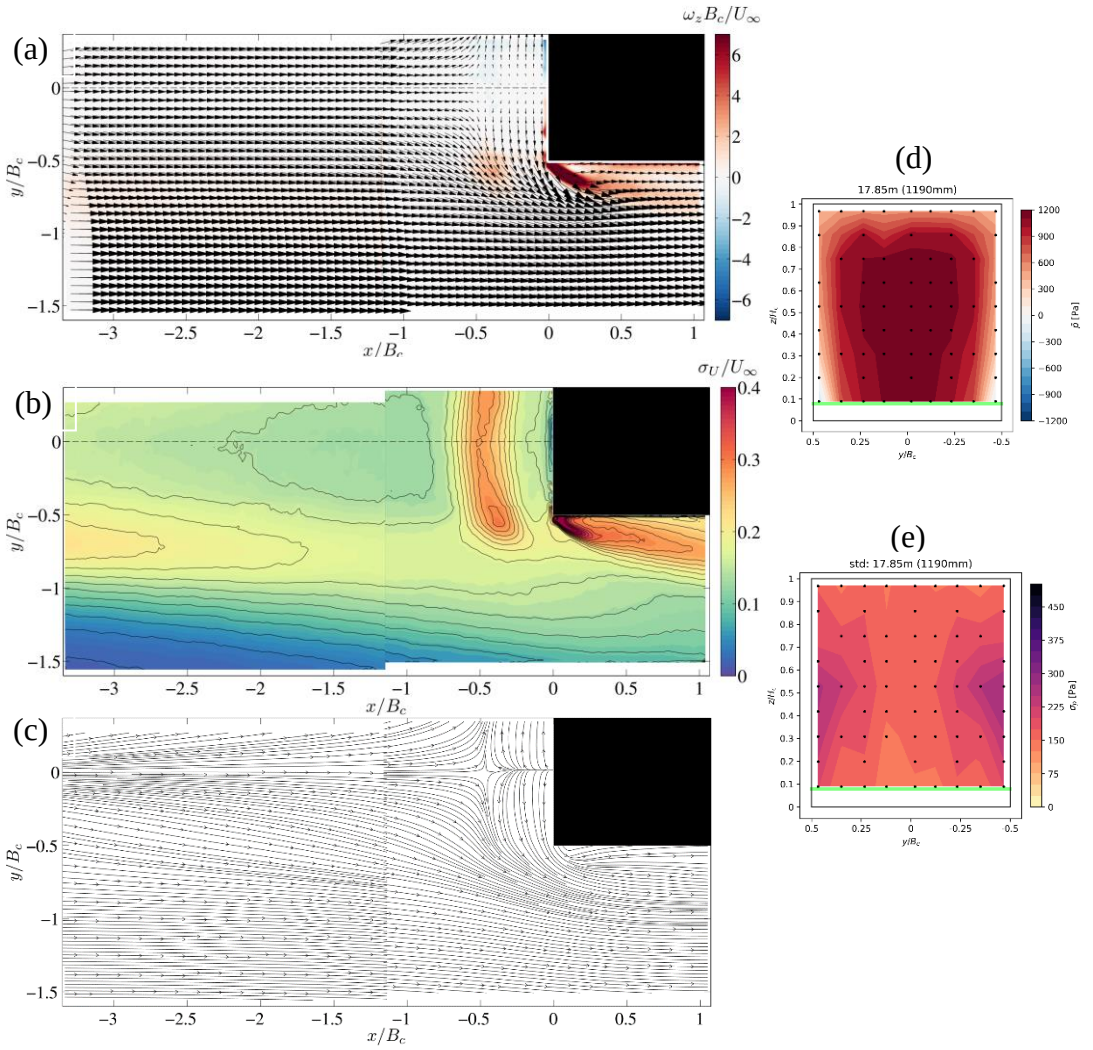


Figure 11: (a) Averaged vector field with colour-coded vorticity $\omega_z$, (b) standard deviation of the absolute velocity, (c) streamlines of the averaged velocity field, (d) averaged surface pressure distribution and (e) standard deviation of the surface pressure distribution for the gap size 17.9 m (model dimension: 1196 mm).

**Gap configuration 10.2 m (model dimension 678 mm ≙ 4.0 $B_c$; Figure 10):**
This gap configuration lies within the range of 1ES and 2ES gap size (cf. Figure 3). For this configuration, the recirculation area downstream of the upstream container is clearly separated from the stagnation point flow upstream of the test container (cf. Figure 10a and c). This results in a significantly expanded separation area and an increased stagnation point flow, which is characterized by a further increase in the averaged surface pressure distribution in the middle of the test container (cf. Figure 10d) and an associated increase in the drag coefficient (cf. Figure 1). The acceleration of the flow at the leading edges of the test container is also increased, whereby the

separation of the flow has shifted somewhat further downstream of the trailing edge (cf. Figure 10a and b).
The existence of a standing vortex upstream of the test container and the stagnation point flow can be observed, which develops due to the near-bottom flow close above the carriage plate (cf. Figure 10b and c). In addition, there is now an increased interaction of the detachment area in the gap with the free inflow, which leads to a widened boundary layer at the level of the test container (cf. Figure 10b). The standard deviation of the surface pressure distribution now shows slightly lower values at the leading edges of the test container than in the previous configuration, as the flow detaches further downstream of the leading edges (cf. Figure 10e).

**Gap configuration 17.9 m (model dimension 678 mm ≙ 7.0 $B_c$; Figure 11):**
This gap configuration corresponds to a gap size of 2ES (cf. Figure 3). For this loading case, the flow within the gap matches approximately the flow case of a free inflow to the test container. This is accompanied by a strong stagnation point flow and a strong acceleration of the flow at the leading edges of the test container, which can typically be observed for the case of a bluff body exposed in a free inflow (cf. Figure 11a and c). The flow now hits the test container completely frontally, which leads to the highest measured average surface pressures in the center of the front surface of the test container of all configurations considered here (cf. Figure 11d). With regard to the drag coefficients, a convergence in the curve can therefore be observed (cf. Figure 1).
The standing vortex upstream of the test container already observed in the previous configuration is still present in a pronounced form and the flow separation at the leading edges of the test container is again shifted further laterally downstream (cf. Figure 11b and c). As a result, the pressure fluctuations in the middle of the front surface of the test container are somewhat reduced, as the flow now hits the front surface frontally and only causes fluctuations at the sides of the front edges (cf. Figure 11e).

# 4 Conclusions and Contributions

The influence of gaps in the loading scheme of a freight train was investigated in a scaled wind-tunnel experiment with regard to the flow structures that occur and the associated aerodynamic drag as well as the surface pressures on a test container. It was possible to categorise different flow situations that are characteristic of the respective loading configuration. For small gaps (<1m), the flow is trapped inside of the cavity and the turbulent boundary layer flow does not interact with flow inside of the gap. With increasing gap size, an increasing inflow into the gap was observed, which causes a coherent reverse flow area in the region of the measuring plane. Reaching a critical gap size of approximately one container leads to a separation of the flow structures within the gap into a recirculation region and a stagnation point flow as well as a greatly increased aerodynamic resistance. Further enlargement of the gap results in an almost free flow towards the test container and an associated maximum value of aerodynamic drag. Future investigations concern the detailed measurement of the flow field in different vertical planes as well as the application of

three-dimensional flow measurement methods. A more detailed investigation of the transient flow and the cross-correlation with simultaneously measured forces are also future objectives.
Based on this investigation, it is possible to quantify optimisation potential in the loading scheme with regard to aerodynamic efficiency. The avoidance or reduction of recirculation areas and strong stagnation point flows by adapting the container geometry or installing flow-influencing structures can be taken into account in future aerodynamic optimizations on the basis of the knowledge gained. Recommendations for gap sizes can also be made in order to increase energy efficiency.

## Acknowledgements

Funded by the European Union. Views and opinions expressed are however those of the authors only and do not necessarily reflect those of the European Union or the Europe's Rail Joint Undertaking. Neither the European Union nor the granting authority can be held responsible for them. The project is supported by the Europe's Rail Joint Undertaking and its members.


# References

[1] Deutsche Bahn AG, "Integrated Report 2022", Berlin, 2022. url: ibir.deutschebahn.com/2022/fileadmin/pdf/db_ib22_e_web.pdf (18/01/2014)
[2] A. Buhr et al., „Aerodynamischer Einfluss von Lücken im Beladungsschema von Güterzügen - Teil 1: Parameterstudie zum Strömungswiderstandbeiwert", STAB-Workshop, Göttingen, 2023.
[3] J. Östh, S. Krajnović, "A study of the aerodynamics of a generic container freight wagon using Large-Eddy Simulation", Journal of Fluids and Structures, 44, 31-51, 2014, DOI: 10.1016/j.jfluidstructs.2013.09.017
[4] C. Li, D. Burton, M. Kost, J. Sheridan, M.C. Thompson, "Flow topology of a container train wagon subjected to varying local loading configurations", Journal of Wind Engineering and Industrial Aerodynamics, 169, 12-29, 2017, DOI: 10.1016/j.jweia.2017.06.011
[5] DIN EN 14067-4:2019-06 (Juni 2019). Bahnanwendungen – Aerodynamik - Teil 4: Anforderungen und Prüfverfahren für Aerodynamik auf offener Strecke